LINEAR POLARIZATION SUM IMAGING IN PASSIVE MILLIMETER-WAVE IMAGING SYSTEM FOR TARGET RECOGNITION

Won-Gyum Kim[1], Nam-Won Moon[1], Hwang-Kyeom Kim[2], and Yong-Hoon Kim[1, *]

[1]Microwave Sensor System Lab, School of Information and Mechatronics, Gwangju Institute of Science and Technology, #123 Cheomdangawiro, Buk-Gu, Gwangju 500-712, Republic of Korea

[2]Defense Acquisition Program Administration, #23 Yongsango-Gil, Yongsan-Dong, Yongsan-Gu, Seoul 140-841, Republic of Korea

Abstract—In passive millimeter-wave imaging systems used indoors, the radiometric temperature contrast is barely enough for coarse object detection, being usually insufficient for recognition due to the absence of cold sky. The image contrast results from a combination of emissivity and reflectivity which are dependent on the dielectric constant of objects, the angle of incidence, and the polarization direction. To improve the capability of target recognition, we proposed the linear polarization sum imaging method which is based on the combination of the different polarization images for increasing the intensity contrast between the target area and the background area. In order to capture the linear polarization sum images of a metal sphere, a metal and a ceramic cup, we designed W-band quasi-optical imaging system which can generate the polarization dependent images by manually changing the linear polarization direction of its radiometer receiver from 0 to $\pi/2$ by the step size of $\pi/8$. The theoretical and experimental results of the linear polarization sum imaging show that it is capable for achieving good image quality enough to recognize the target.

1. INTRODUCTION

Millimeter-wave systems have been used for various applications for military, radio astronomy, security, medicine, inspection, and meteorology applications because it has the advantages of low atmospheric attenuation and high penetrability into thin building wall and fabric barriers such as hair and clothing. Passive millimeter-wave (PMMW) imaging systems generate interpretable images in bad weather and low-visibility conditions such as haze, smoke, sandstorms, fog, and clouds through the passive detection of naturally occurring millimeter-wave radiation from an object [1–3]. Objects reflect and emit radiation in the millimeter-wave regime, just as they do in the IR and visible regimes. The degree to which an object emits is characterized by its emissivity which is a function of the dielectric constant, the incident angle of radiation and the polarization like Fresnel's reflectivity [3]. In outdoor imaging, the sky is usually 100–200 K cooler than the ambient temperature in the millimeter-wave region this means that metal objects appear very strongly due to the reflection of the cold sky. However, in indoor imaging, objects can effectively disappear because they reflect the ambient temperature in the absence of the sky. It means that the indoor PMMW image shows the low temperature contrast between the target and the background which is insufficient to recognize the target [4, 5]. In general, active systems are used to improve the image contrast and they usually exploit coherent illumination which causes the source of significant interference effects or speckle [6, 7]. Polarimetric imaging is also one of the methods used to enhance the target discriminability because using polarization diversity allows one to obtain additional information on the shape and material of the surface and can be an additional parameter for the recognition of objects on the basis of their radio images in the millimeter-wave range [8–10]. The past research on polarimetric imaging focused on the dual-polarized or multi-polarized images for active imaging systems [11–14]. Polarization difference imaging (PDI) has been recently researched as a method of imaging in optically scattering media and it typically uses the difference signal between the orthogonal linear polarization images of an active imaging system [15–17]. So far, there are few studies on the polarimetric imaging for PMMW imaging systems especially operated in indoors. In this paper, we proposed a linear polarization sum imaging (LPSI) which evenly increases intensities of pixels in a target image by combining three or more polarization images for the PMMW imaging system. Preliminary tests on a few samples are implemented by the designed millimeter-wave imaging system in-doors. The results show

the potential of using the imaging method in PMMW imaging system for target recognition.

This paper shows the concept of the linear polarization sum imaging in a PMMW imaging system in Section 2. In Section 3, we present the design and performances of PMMW quasi-optical imaging system. The experimental results of the linear polarization sum imaging are shown in Section 4. Conclusion follows in Section 5.

2. LINEAR PLARIZATION SUM IMAGING IN PMMW IMAGING SYSTEM

Passive millimeter-wave imaging is a method of forming images through the passive detection of naturally occurring millimeter-wave radiation from a scene. Objects reflect and emit radiation in the millimeter-wave regime, just as they do in the IR and visible regimes. The degree to which an object reflects or emits is characterized by the emissivity of the object. The emissivity of an object is a function of the polarization, the dielectric properties of its constituents, its surface roughness, and the angle of observation. When an object's physical thermodynamic temperature (T_o) is multiplied by its emissivity (ε), the resultant product is defined as the object's surface brightness or radiometric temperature (T_s),

$$T_s = \varepsilon \cdot T_o. \tag{1}$$

The variation in emissivity of common scene materials is an important factor in the generation of scene images by causing variations in the power radiated from different parts of the scene. If this were the only factor involved, the images could be formed by simply mapping measured values of T_s in the scene. However, the way the scene is illuminated is critical in the way the scene actually looks. If an object is a metal plate with $\varepsilon = 0$, it will have $T_s = 0$, but, because it is highly reflective, it will have the radiometric temperature of whatever object it is reflecting. This effect is captured by a surface scattered radiometric temperature (T_{sc}) defined as the product of the object's reflectivity and the radiometric illumination temperature (T_{ill}) of whatever happens to be illuminating it as follows

$$T_{sc} = r \cdot T_{ill}. \tag{2}$$

Combining the terms T_s and T_{sc} gives the effective radiometric temperature T_e of the object,

$$T_e = T_s + T_{sc} = \varepsilon \cdot T_o + r \cdot T_{ill}. \tag{3}$$

It is important to note that the emissivity ε and the reflectivity r are related through Equation (4),

$$r = 1 - \varepsilon. \tag{4}$$

Moreover, these two coefficients depend on the physical characteristics of the materials defined via the frequency (f), the dielectric constant (n), the angle of incident (θ), and the polarization (p). Since the source is incoherent, the two coefficients in Equation (3) are added. Obtaining Equation (3) describes the received temperature at the input of the sensor as follows

$$T_{rec}(f, n, \theta, p) = \varepsilon(f, n, \theta, p) \cdot T_o + r(f, n, \theta, p) \cdot T_{ill}. \qquad (5)$$

The reflection coefficient, shown in Equation (5), can be separately represented for the horizontal and the vertical polarization case following Fresnel's law,

$$\varepsilon_h(f, n, \theta) = 1 - r_h(w, n, \theta) \qquad (6)$$
$$\varepsilon_v(f, n, \theta) = 1 - r_v(w, n, \theta). \qquad (7)$$

Imaging can be accomplished by measuring incoherent T_{rec} as a function of position in the scene, thus creating a two-dimensional (2-D) image of the scene. The resulting image can be modeled as combinations of an unpolarized component and a completely polarized component, which produce a partially polarized image. The combined shape of these two components can be described by the equation of an ellipse. Assuming that we use a perfect linear polarizer, the quasi-optical imaging system shown in Section 3, with the angle (φ) being the polarization direction of the sensor, and θ being the orientation angle of the major axis of the polarization ellipse, then the observed pixel brightness (I) can be described as

$$I = U + A \cdot \cos\left[2 \cdot (\theta - \varphi)\right]. \qquad (8)$$

The sensor with the unpolarized characteristic has the detected pixel value of $2U$. The quantity "degree of linear polarization" is defined as $p = A/U$. If three different polarization directions are used to capture three images of the same scene, we can recover the parameters A, U, which give a generalized picture of the polarization features of the scene. Having three pictures of the scene: I_0, I_{45}, I_{90}, with polarizer oriented at $\varphi = 0$, 45 and 90 with respect to the horizon as a reference direction, we can get the parameters of Equation (8) as follows

$$\begin{aligned} U &= (I_0 + I_{90})/2 \\ A &= \sqrt{(I_{45} - U)^2 + (I_{90} - U)^2} \\ \theta &= \arctan\left[(I_{45} - U)(I_0 - U)\right]/2 \end{aligned} \qquad (9)$$

Here the meaningful range of θ is 0 to π because θ and $\theta + \pi$ are indistinguishable for a phase-blind visual sensor. Additionally, we

can have linear polarization sum imaging (LPSI) which has intensity defined as

$$I_{PS} = \frac{1}{3} \left(I_{90} + I_{45} + I_0 \right). \tag{10}$$

Ideally, an image based on Equation (10) is equivalent to one obtained by a polarization-blind imaging system that measures the summation of polarization dependent intensities. Such a polarimetric imaging technique using the different polarization dependent images leads to a higher intensity contrast between an object and a background than that of a single linear polarization image.

3. PMMW QUASI-OPTICAL IMAGING SYSTEM DESIGN

The configuration and signal flow of PMMW radiometer imaging system is shown in Figures 1 and 2. The imaging system consists of quasi-optics, a radiometer receiver, a scanner, and a PC. The key design requirements of the imaging system are the temperature resolution of below $1\,\mathrm{K}$, the spatial resolution (SR) of about $0.45°$, and the field of view (FOV) of above $10° \times 10°$ in the W-band.

The quasi-optics are composed of a lens, a reflector and a feeder, which have the role of focusing the incident millimeter-wave radiation from an object in a scene to a radiometer receiver positioned on the focal plane. The aspheric convex-convex lens as a focusing element and the flat metal reflector as a mirror are designed at the center
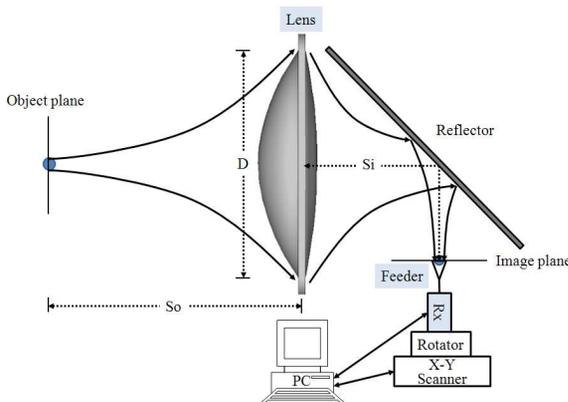

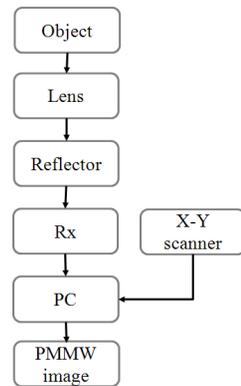**Figure 1.** Configuration of PMMW quasi-optical imaging system.

Figure 2. Signal flow of imaging system.

frequency of 94 GHz using CODE V optical design simulator. The design focuses on achieving wide frequency bandwidth, high resolution and low blurring as well as having a compact size. The quasi-optical lens has the aperture diameter (D) of 500 mm in order to satisfy the required spatial resolution with the condition of having an effective focal length (F) of 500 mm, with a corresponding F-number of 1. The lens is fabricated from high density polyethylene (HDPE) with the refractive index of 1.5187 at 94 GHz for the reduction of weight and dielectric loss using a 3D super precision machine. The reflector, which is made from an aluminum plate with good surface roughness, has a circular shape with the thickness of 10 mm and a diameter of 500 mm which is the optimum size to minimize the spillover loss between the lens and the feed antenna at the limited space of the quasi-optics. The dielectric rod antenna (DRA) as a feed antenna or a receiver antenna was designed by CST Studio simulator to achieve low return loss and high efficiency for good quasi-optical transmission efficiency between it and the lens. The feeder is composed of a tapered dielectric rod and a WR-10 standard waveguide. Using a 3D molding machine, the sharp dielectric bar was also fabricated from the same HDPE material used for the quasi-optical lens for good impedance matching. The fabricated DRA is measured by near-field measurement equipment to get the radiation beam pattern on the H-plane. The measured beam pattern has the gain of 15.3 dB, the first side lobe level of below -18 dB and 10 dB beam-widths of 51.3° at 94 GHz. We tested the quasi-optics without the metal reflector using far-field measurement equipment to obtain the focused H-plane beam pattern at 90, 94 and 98 GHz. The measured beam patterns have the 3 dB spot size of about 3 mm for all frequencies. The detailed configuration, test method and measurement results of the quasi-optics are described in the previous paper, Reference [18].

The radiometer receiver is based on a direct conversion total power radiometer due to its high temperature sensitivity and simple structure. The receiver mainly consists of an RF unit, an LF unit, and
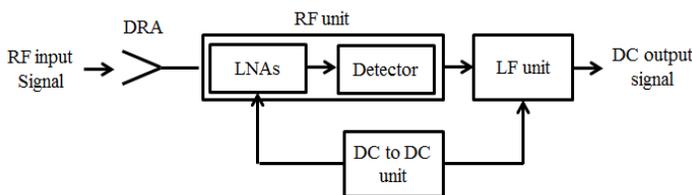

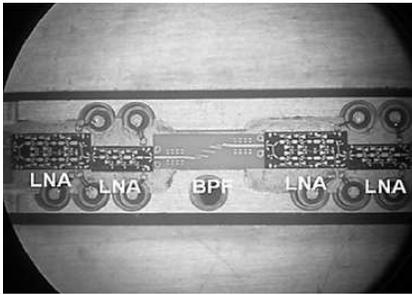
Figure 3. Block diagram of W-band radiometer receiver.

Figure 4. Photo of fabricated 4-stages low noise amplifier. (Courtesy by millisys Inc.).
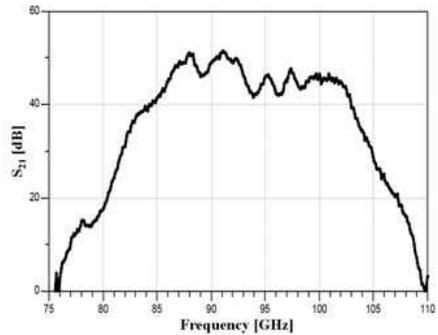

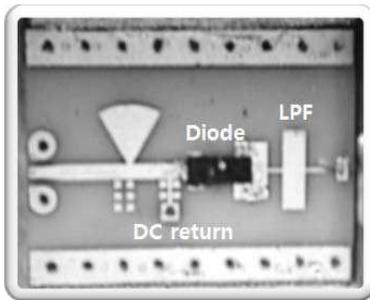**Figure 5.** Measured gain of multi-section LNAs.

Figure 6. Photo of fabricated Schottky based diode based detector. (Courtesy by millisys Inc.).
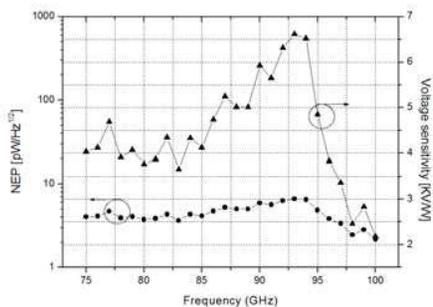

Figure 7. Measurement results of square law detector.

a DC to DC unit as shown in Figure 3. The key RF part includes the designed dielectric rod antenna, 4-stage low noise amplifiers (LNAs) and square law detector to amplify the RF input signal level within the in-band and to convert the RF signal to DC signal for signal processing. As shown in Figure 4, the multi-section LNAs is manufactured with two 2-stage LNAs, which were assembled with two commercial MMIC LNAs supplied by Northrop Grumman, to increase the received signal above the detector noise floor and a designed thin film band pass filter (BPF), which was inserted between two LNA pairs, to prevent oscillation and improve gain flatness. Figure 5 shows the experimental results of the assembled LNA with a bandwidth of about 10 GHz and

an average gain of more than 45 dB within the receiver bandwidth. The RF detector is designed as a Schottky diode based detector with zero bias because of its simple structure and low $1/f$ noise. As shown in Figure 6, the detector was fabricated by mounting a Diode from Virginia Diodes Inc. on the designed thin film circuit which contains an input matching network and an output low pass filter (LPF). The measurement results of voltage sensitivity and noise equivalent power (NEP) are around $4.8\,\mathrm{kV/W}$ and $3.0\,\mathrm{pW/Hz}^{1/2}$ at 95 GHz as shown in Figure 7.

The fabricated radiometer has a T-shaped structure to easily extend the receiver channel for a focal plane array imaging system. The measured temperature sensitivity of the receiver is 0.7 K and 1.0 K for cold and hot calibration source during 60 ms, respectively [19].

The scanner is constructed from an XY scanner and a Z-axis scanner. The XY scanner is composed of a two-step motor with the position accuracy of below 0.01 mm. The receiver is mounted on the top stage of the Z-axis scanner which can be manually scanned within the range of 40 mm. The XY scanner automatically moves the receiver for forming a 2D image after putting the receiver on the optimum focal plane by positioning the Z-axis stage.

The PC as a signal processing unit mainly consists of a data acquisition (DAQ) board and graphic user interface (GUI). It finally makes a PMMW 2D image in 256 gray levels by processing the output signal of the radiometer receiver. The commercial PCI-911HR was used for DAQ board with a sampling rate of 100 kHz and a resolution of 16 bits. The programmed GUI software has two main roles: displaying the W-band electromagnetic wave image and controlling the radiometer imaging system.

4. MEASUREMENT RESULTS OF LINEAR POLARIZATION SUM IMAGING

In order to generate linear polarization images we use the PMMW quasi-optical imaging system, mentioned in Section 3, with a single linear polarization characteristic. Figures 8 and 9 show the experimental environment and image processing flow of the PMMW imaging system in obtaining a linear polarization sum (LPS) image. The different polarization images are simply measured by manually rotating the polarization angle of the radiometer receiver of the imaging system, though they are not synchronized. To get the LPS image, we first capture three different polarization raw images whose intensity distribution are represented by $I_{\theta n}(x,y)$, where $(x,\ y)$ identifies the position on the image and the symbol θ_n represents n-th polarization
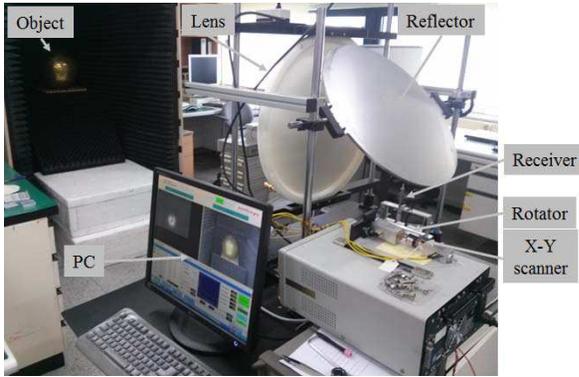
Figure 8. Experiment environment of LPSI using PMMW quasi-optical imaging system. (Courtesy by millisys Inc.).
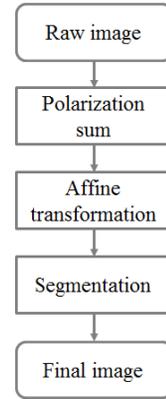
Figure 9. Image processing flow of linear polarization sum imaging.

angle with respect to the vertical direction. The measured intensity distribution of the LPSI are formed as

$$I_{LPSI}(x,y) = \frac{1}{m} \sum_{n=1}^{m} I_{\theta n}(x,y). \tag{11}$$

After the LPSI of a scene are formed, it is desirable to display them in a way that optimizes the use of the available dynamic range of the imaging system. This makes it easier to locate small intensity variations within a scene. We carry out this process by applying an affine transformation to the intensity distribution of the LPSI. Specifically, we determine the transformed quantity,

$$I_{LPSI}(x,y)_{trans} = \kappa_{LPSI} \left[I_{LPSI}(x,y) - I_{LPSI}(x,y)_{\min} \right], \tag{12}$$

The quantity on the left-hand side of Equation (12) is the LPSI transformed for optimal display. $I_{LPSI}(x,y)_{\min}$ represents the smallest value of intensity in the original LPSI and κ_{LPSI} is the stretching factor, defined as

$$\kappa_{LPSI} = C / \left[I_{LPSI}(x,y)_{\max} - I_{LPSI}(x,y)_{\min} \right] \tag{13}$$

where C is the maximum available receiver output level.

The simple, four-step process of capturing three raw images, adding them, and transforming the resulting sum image can be implemented rapidly for LPSI. We chose the affine transformation because it is logical, linear, and easy to implement. By applying

the specific affine transformations defined in Equation (13), we can use the entire available dynamic range of the receiver without losing any information contained in the raw images. Additionally, the interpolation processing is used for improving the image resolution and then Otsu's method is applied to image segmentation processing for good discrimination between objects and their surrounding background by selecting the threshold value which maximizes the between-class variances of the histogram.

In this paper, all raw images are obtained by PMMW quasi-

(a)

(b)
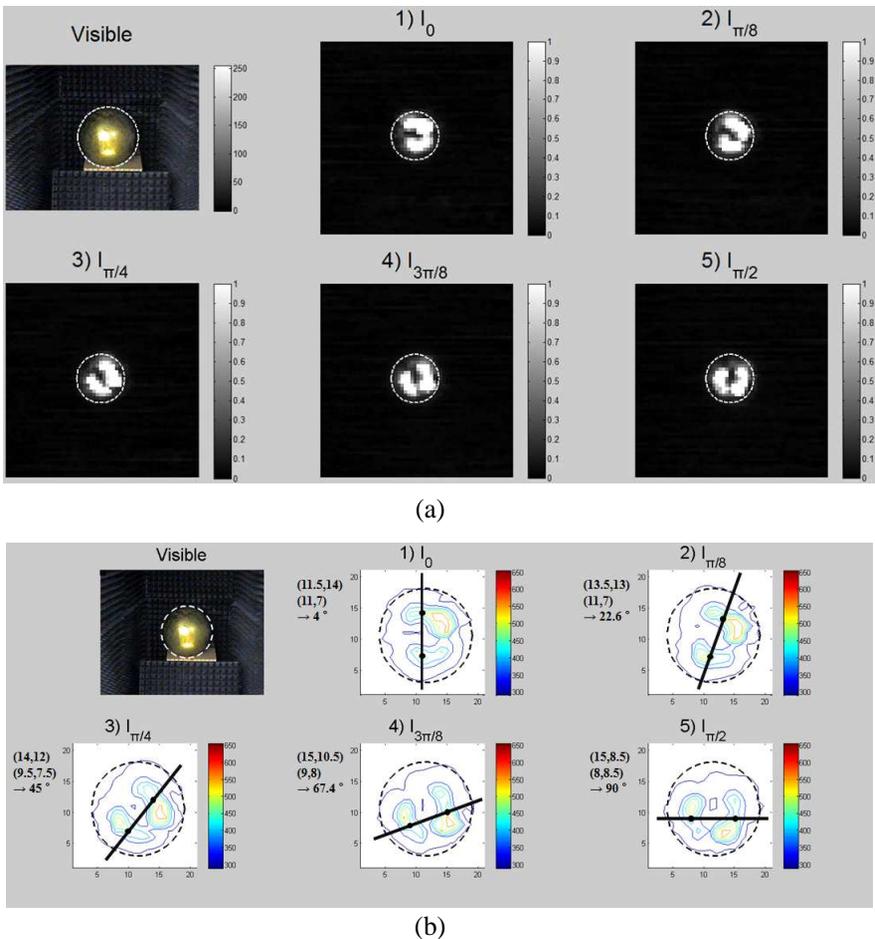
Figure 10. PMMW raw images of metal sphere via linear polarization direction: (a) gray-level image, (b) temperature contour image.

optical imaging system with the condition that the object distance, S_o, between an object and the lens is 2500 mm and the image distance, S_i, from the lens to the receiver through the metal reflector is about 500 mm. The test objects are surrounded by electromagnetic absorbers for the reduction of the environmental noise which degrade the image quality. Additionally, the scanning area is 90 mm × 90 mm with the step size of 1.5 mm, corresponding to a 60 × 60 image resolution, to cover the scene of interest. In order to capture five polarization images, the receiver polarization angle, θ, is varied from 0 to $\pi/2$ with the step size of $\pi/8$ by rotating the rotator on which the radiometer receiver is mounted. The post-processing from polarization sum to segmentation via affine transformation is done by MATLAB R2010a. The interpolated image is 480 × 480 corresponding to eight times of the 60 × 60 raw images. For the image segmentation based Otsu's method, the function supplied by MATLAB was used.

Before verifying the linear polarization sum imaging, first we analyzed the effects of the receiver polarization angle on the passive millimeter-wave images. The polarization-dependent PMMW images of a metal sphere, which is usually used as a standard target for microwave remote sensing applications, are measured by the developed quasi-optical imaging system while varying the receiver polarization angle with the rotation step of $\pi/8$. As shown in Figure 10, the measured raw images of the sphere are described as the gray-level and temperature contour type to provide ease in analyzing the polarimetric characteristics. The temperature images are especially transformed from the raw voltage data with the receiver calibration data which is obtained by using the two point calibration method with absorbers at a room temperature of 290 K and liquid nitrogen of 77 K. The sphere with the diameter of 30 cm should be shown in a PMMW image with the pixel number of about 8 because the imaging system has the spatial resolution of about 2 cm at the image distance of 2.5 m and it is indicated by a dotted line in Figure 10.

As shown in Figure 10(a), the measured PMMW images of the metal sphere show that a PMMW single polarization image has fewer pixel numbers than the expected values indoors making it difficult to recognize an object. Figure 10(b) shows that the degree of image rotation almost follows the receiver polarization angle which proves that the PMMW images are dependent on the polarization as shown in Equation (5). Additionally, the temperature contour images show that the metal sphere has the maximum temperature of 563 K which is the saturation level. To verify the superior performance of the linear polarization sum imaging and to find the optimum polarization combination for LPSI, the various LPS images with the different
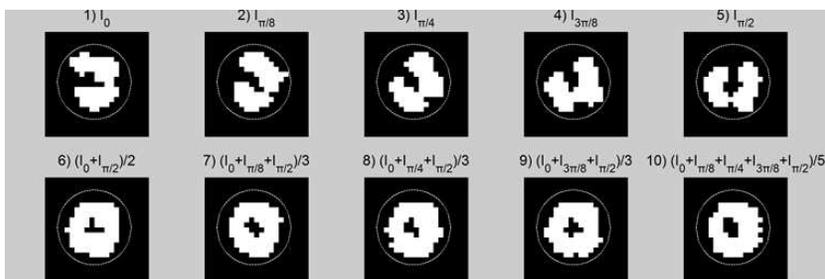
(a)
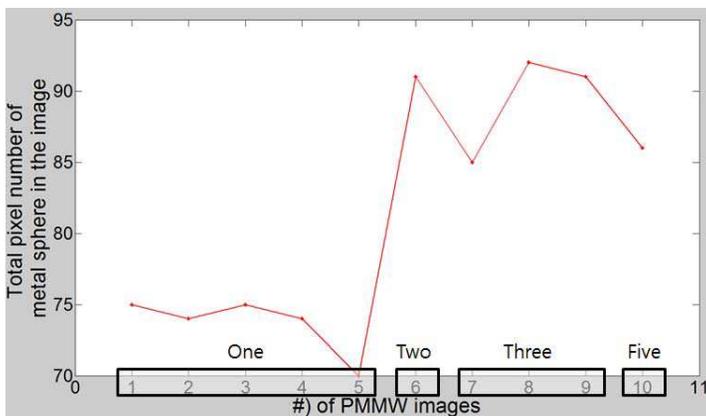
(b)
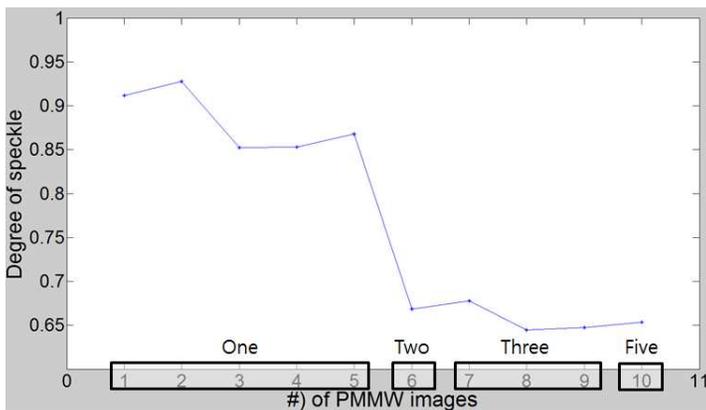
(c)

Figure 11. Comparison between PMMW single polarization and LPS images of metal sphere: (a) polarization images, (b) total pixel number, (c) degree of speckle.

polarization sets are obtained as shown in Figure 11(a). The LPS images are normalized in accordance with Equation (11) for the comparison with the single polarization images. The pixel numbers of the sphere for each PMMW images are shown in Figure 11(b). The numbers at the bottom of Figure 11(b) are same to the numbers at the top of images in Figure 11(a). The numbers 1 to 5 are the single polarization images, 6 is the LPS image summed with two images, 7 to 9 and 10 are the LPS images summed with three and five images. In the side of the pixel count, the results show that LPSI method gives better visibility than the general imaging scheme with the improvement of more than 15% and case 8 offers the best performance for the metal sphere. As shown in Figure 11(c), the degree of speckle (DOS) is used to quantitatively analyze the degree of an image quality enhancement of the LPSI. The DOS on the target image can be described by the ratio of standard deviation and mean value of the target image as follows [20].

$$DOS = \frac{\sqrt{\frac{1}{N} \sum_{k=1}^{N} \left(I_k - \bar{I}\right)^2}}{\bar{I}}$$
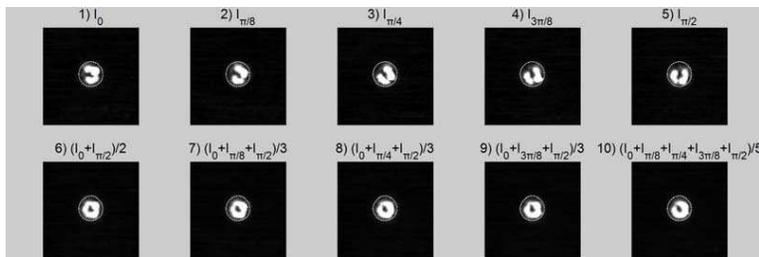
(a)
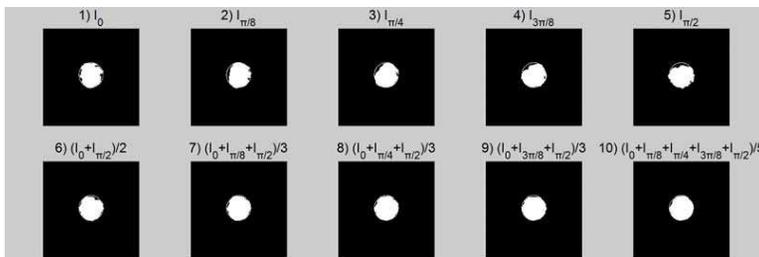
(b)

Figure 12. PMMW post-processing of single polarization and LPS images of metal sphere: (a) interpolation image, (b) final image.

where I_k is the amplitude of the k-th pixel on the target image. N is the total number of pixels within the target area on the acquired image. $\bar{I}$ is the mean value of the target image: $\frac{1}{N} \sum\limits_{k=1}^{N} I_k$. In the side of the DOS, the results show that LPSI offers better image quality than the single polarization image with the improvement of more than 23% and case 8 also gives the best performance for the metal sphere. As shown in Figure 12, the post-processing images, i.e., interpolation
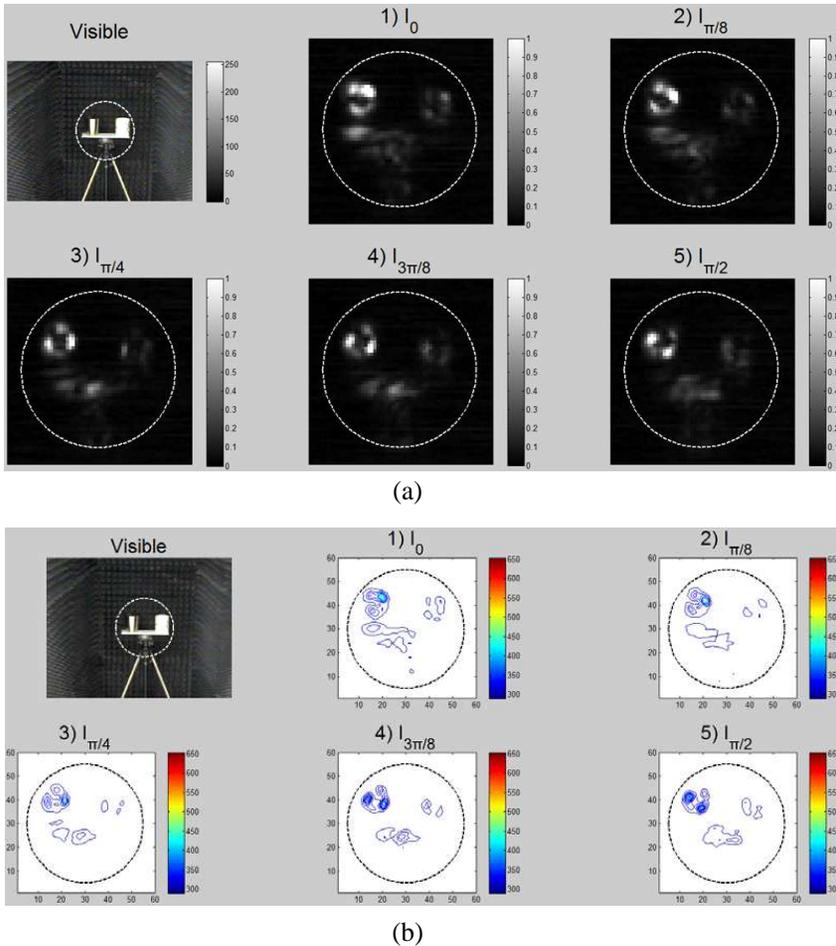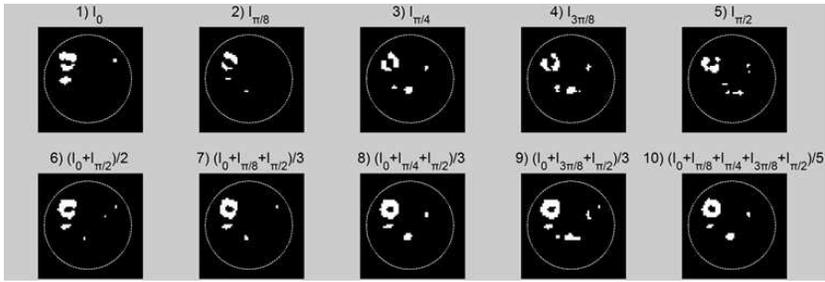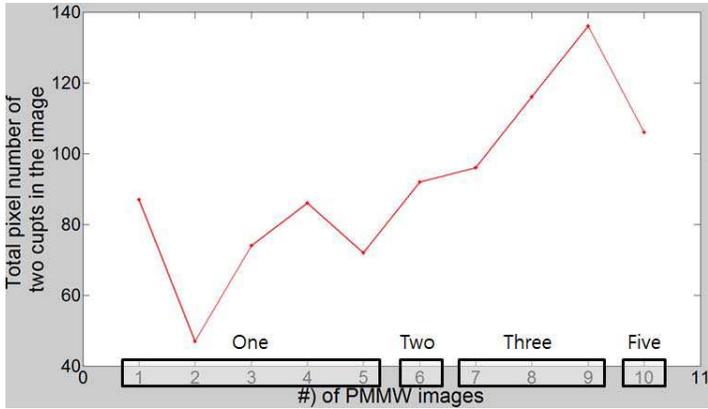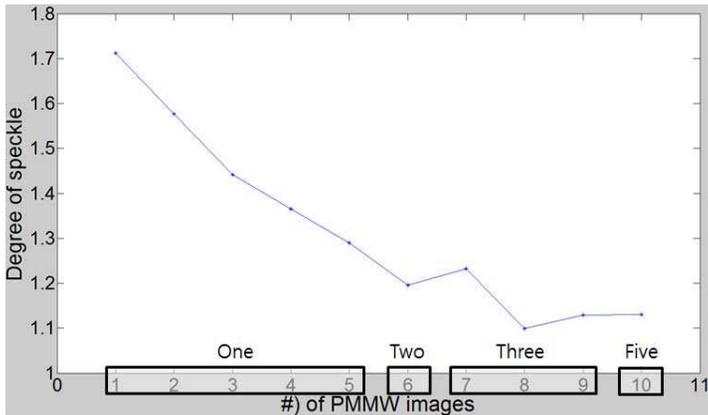

(a)

(b)

Figure 13. PMMW raw images of metal cup (left) and ceramic cup (right) via linear polarization direction: (a) gray-level image, (b) temperature contour image.

(a)

(b)

(c)

Figure 14. Comparison between PMMW single polarization and LPS images of two cups: (a) polarization images, (b) total pixel number, (c) degree of speckle.

and final LPS images, demonstrate that the LPS images with two or more polarization images of the metal sphere have almost the same visibility but a slight different in shape.

The same image acquisition procedure for LPSI, as mentioned above, is also applied in obtaining the LPS images of two cups made of different material and shape. Figure 13 displays the PMMW raw images of the metal and ceramic cups through the receiver polarization angle. The captured images show the same polarization phenomenon like that of the metal sphere case shown in Figure 10. Figure 13(a) shows that the single polarization images are not clear enough to recognize two cups. As shown in Figure 13(b), the metal cup has the temperature range of $290\,\mathrm{K}$ to $480\,\mathrm{K}$. The temperature difference between the metal sphere and the metal cup is mainly caused by the different surface shape and size. Moreover, the results show that the metal cup image is brighter than that of the ceramic cup because of the higher Fresnel's reflection coefficient which is primarily due to the high conductivity and free electrons. To reaffirm the superior performance of the LPSI, the various LPS images of the cups with the different
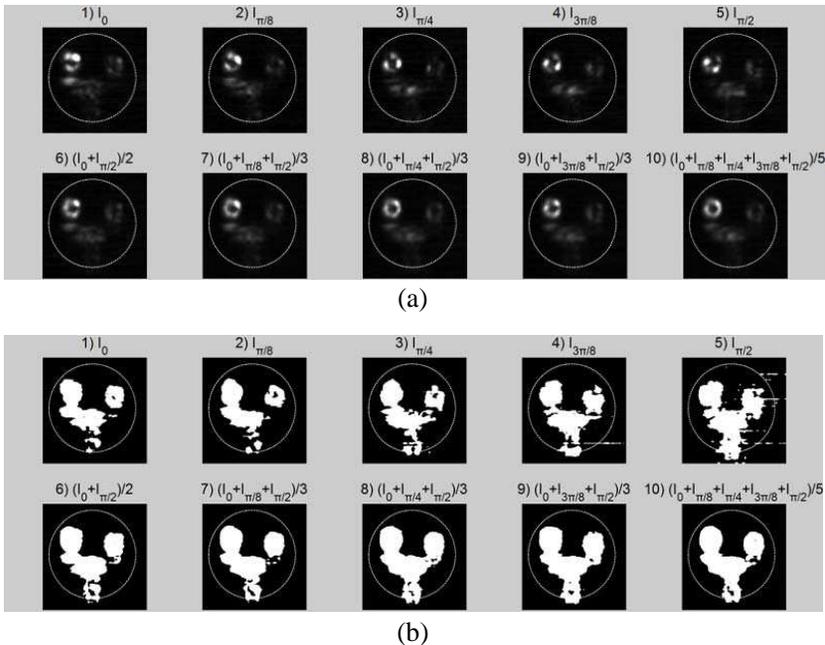

(a)

(b)

Figure 15. PMMW post-processing of single polarization and LPS images of two cups: (a) interpolation image, (b) final image.

polarization combination are obtained as shown in Figure 14. In the side of the pixel count, LPSI scheme gives the improvement of more than 30% compared to the single polarization image and case 9 has the best performance for the metal and ceramic cup. From the *DOS* perspective, LPSI shows the improvement of 16% to 25% compared to the single polarization image and case 8 offers the best performance for the cups. The LPS images of the cups through the interpolation and image segmentation processing are shown in Figure 15. The measured LPS images obtained from two or more polarization images of the cups have higher visibility and quality than the single polarization images. Moreover, the results indicate that the visibility of the LPSI of the ceramic cup is more sensitive to the polarization combination compared to that of the metal cup.

5. CONCLUSIONS

The linear polarization sum imaging is proposed to improve the PMMW image quality for target recognition indoors. The concept of the imaging method is based upon the idea that the radiometric temperature of an object at the input of the imaging system is dependent on the polarization angle of the radiometer receiver that leads to the polarization dependent image. In order to verify linear polarization sum imaging we designed W-band quasi-optical radiometer imaging system which mainly consists of a quasi-optical lens antenna with the aperture size of $50\,cm$ and a radiometer receiver with the temperature resolution of less than $1\,K$. The experimental results show that PMMW image has different information with respect to the electrical and physical characteristic of an object and the polarization direction. It is also confirmed that the linear polarization sum imaging with three polarization images is sufficient for ordinary objects to obtain PMMW images with good visibility and image quality.

REFERENCES

1. Yeom, S., D. S. Lee, H. Lee, J. Y. Son, and V. P. Guschin, "Distance estimation of concealed objects with stereoscopic passive millimeter-wave imaging," *Progress In Electromagnetics Research*, Vol. 115, 399–407, 2011.

2. Wikner, D. A. and A. R. Luukanen, *Passive Millimeter-wave Imaging Technology XIV*, Orlando, Florida, United States, SPIE, Bellingham, Wash., Apr. 28, 2011.

3. Ulaby, F. T., R. K. Moore, and A. K. Fung, *Microwave Remote Sensing: Active and Passive, Volume I: Fundamentals and Radiometry*, Artech House Publishers, 1981.

4. Lynch, J. J., H. P. Moyer, J. H. Schaffner, Y. Royter, M. Sokolich, B. Hughes, Y. J. Yoon, and J. N. Schulman, "Passive millimeter-wave imaging module with preamplified zero-bias detection," *IEEE Transactions on Microwave Theory and Techniques*, Vol. 56, 1592–1600, Jul. 2008.

5. Zhang, G. F., X. G. Li, and G. W. Lou, "Research on passive MMW imaging based on an alternating current radiometer," *Journal of Infrared and Millimeter Waves*, Vol. 26, 461–464, Dec. 2007.

6. Qi, F., V. Tavakol, D. Schreurs, and B. Nauwelaers, "Limitations of approximations towards fourier optics for indoor active millimeter wave imaging systems," *Progress In Electromagnetics Research*, Vol. 109, 245–262, 2010.

7. Zhang, L. X., J. Stiens, A. Elhawil, and R. Vounckx, "Multispectral illumination and image processing techniques for active millimeter-wave concealed object detection," *Applied Optics*, Vol. 47, 6357–6365, Dec. 1, 2008.

8. Salmon, N. A., R. Appleby, and P. Coward, "Polarimetric passive millimetre wave imaging," *International Conference on Microwave and Millimeter Wave Technology Proceedings*, 540–543, Aug. 2002.

9. Duric, A., A. Magun, A. Murk, C. Matzler, and N. Kampfer, "The fully polarimetric imaging radiometer SPIRA at 91 GHz," *IEEE Transactions on Geoscience and Remote Sensing*, Vol. 46, 2323–2336, Aug. 2008.

10. Stahli, O., C. Matzler, A. Murk, and N. Kampfer, "Sky measurements with the imaging polarimeter SPIRA at 91 GHz," *Microwave Radiometry and Remote Sensing of the Environment*, 181–186, Mar. 2010.

11. Sugimoto, M. and K. Ouchi, "Extraction of laver cultivation area using SAR dual polarization data," *PIERS Proceedings*, 952–956,

Moscow, Russia, Aug. 19–23, 2012.

12. Liao, S. L., N. Gopalsami, T. W. Elmer, E. R. Koehl, A. Heifetz, K. Avers, E. Dieckman, and A. C. Raptis, "Passive millimeter-wave dual-polarization imagers," *IEEE Transactions on Instrumentation and Measurement*, Vol. 61, 2042–2050, Jul. 2012.

13. Shao, W. and R. S. Adams, "Multi-polarized microwave power imaging algorithm for early breast cancer detection," *Progress In Electromagnetics Research M*, Vol. 23, 93–107, 2012.

14. Teng, H. T., H. T. Ewe, and S. L. Tan, "Multifractal dimension and its geometrical terrain properties for classification of multiband multi-polarized SAR image", *Progress In Electromagnetics Research*, Vol. 104, 221–237, 2010.

15. Miller, D. A. and E. L. Dereniak, "Selective polarization imager for contrast enhancements in remote scattering media," *Applied Optics*, Vol. 51, 4092–4102, Jun. 20, 2012.

16. Sutkowski, M., P. Garbat, J. Parka, A. Walczak, E. Nowinowski-Kruszelnicki, and J. Woznicki, "Polarization difference imaging system with LC filter," *Molecular Crystals and Liquid Crystals*, Vol. 495, 403–411, 2008.

17. Jiang, X. Y., N. Zeng, Y. H. He, and H. Ma, "Investigation of linear polarization difference imaging based on rotation of incident and backscattered polarization angles," *Progress In Biochemistry and Biophysics*, Vol. 34, 659–663, 2007.

18. Thakur, J. P., W. G. Kim, and Y. H. Kim, "Large aperture low aberration aspheric dielectric lens antenna for W-band quasi-optics," *Progress In Electromagnetics Research*, Vol. 103, 57–65, 2010.

19. Kim, W. G., N. W. Moon, J. M. Kang, and Y. H. Kim, "Loss measuring of large aperture quasi-optics for W-band imaging radiometer system," *Progress In Electromagnetics Research*, Vol. 125, 295–309, 2012.

20. Jaeger, I., L. Zhang, J. Stiens, H. Sahli, and R. Vounckx, "Millimeter wave inspection of concealed objects," *Microwave and Optical Technology Letters*, Vol. 49, 2733–2737, 2007.